



## **Beyond-Decade Ultrawideband Quad-Ridge Flared Horn With Dielectric Load From 1 to 20 GHz**

Downloaded from: <https://research.chalmers.se>, 2025-02-01 14:51 UTC

Citation for the original published paper (version of record):

Flygare, J., Yang, J., Pollak, A. et al (2023). Beyond-Decade Ultrawideband Quad-Ridge Flared Horn With Dielectric Load From 1 to 20 GHz. IEEE Transactions on Antennas and Propagation, 71(3): 2110-2125. <http://dx.doi.org/10.1109/TAP.2023.3234708>

N.B. When citing this work, cite the original published paper.

© 2023 IEEE. Personal use of this material is permitted. Permission from IEEE must be obtained for all other uses, in any current or future media, including reprinting/republishing this material for advertising or promotional purposes, or reuse of any copyrighted component of this work in other works.

# Beyond-decade Ultra-wideband Quad-ridge Flared Horn with Dielectric Load from 1 to 20 GHz

Jonas Flygare, *Member, IEEE*, Jian Yang, *Senior Member, IEEE*, Alexander W. Pollak, Robert E. J. Watkins, Fiona Hillier, Leif Helldner, and Sven-Erik Ferm

**Abstract**—In this paper we present a novel dielectrically loaded Quad-ridge Flared Horn (QRFH) as a reflector feed with beyond-decade ultra-wideband performance. The dielectric is machined in a low-loss, space-grade polyimide specified with low outgassing for vacuum environment. The feed covers 1-20 GHz bandwidth with a measured band-average input reflection of  $-13.6$  dB, and 41.5 dB isolation between two orthogonal polarized ports. Predicted performance in a paraboloidal reflector with 60-degree half-subtended angle is 62% aperture efficiency average over the band. The ridges of the horn are designed with analytic-spline-hybrid 3D-profiles with thickness flaring outwards towards the feed aperture, improving low-frequency polarization properties. The QRFH was manufactured in four quarters for accurate ridge-to-ridge alignment and a reduced number of interfaces for good thermal properties in cryogenic applications. A prototype feed has been installed and tested with promising results in one of the 6 m offset Gregorian reflectors of the Allen Telescope Array (ATA) located at the Hat Creek Observatory, CA, USA.

**Index Terms**—ultra wideband antennas, quad-ridge flared horn, dielectric materials, radio astronomy, reflector feed

## I. INTRODUCTION

In broadband radio astronomy whether continuous, spectral line search, or simply monitoring a wide frequency range for detection, the ultra-wideband (UWB) reflector feed is the crucial first component in the antenna receiver chain, followed by the low-noise amplifier (LNA). Depending on the application requirements, a trade-off is often made between larger bandwidth and higher absolute sensitivity per Hertz. The trade-off is not always science-motivated but instead by the cost, complexity, and volume reduction from covering a wideband frequency range with a single receiver instead of multiple octave bands. For large arrays such as the Square Kilometer Array (SKA) [1], the next generation Very Large Array (ngVLA) [2], and the Allen Telescope Array (ATA) [3], the UWB feed system is a crucial component. The same applies to the very long baseline interferometry (VLBI) global observing system (VGOS) [4]. State-of-the-art UWB feed designs exist in a variety of concepts, typically based on either log-periodic geometry [5]–[8] or waveguide [9], [10]. The Quad-ridge Flared Horn (QRFH) is a popular choice due to its robustness, low-loss, and ease of manufacturing with standard techniques [10]–[12]. The waveguide structure gives it an intrinsic low-frequency radio-frequency interference (RFI) protection with a sharp cut-off. The QRFH is preferred in single-ended 50- $\Omega$  configuration with only two LNAs required and no additional baluns needed. This configuration has been



Fig. 1: QRFH and the polyimide load insert (magnified).

shown to effectively cover bandwidth ratios from 3:1 to 7:1 with good performance in both illumination and return loss from UHF-band [13] to V-band [14]. The drawback of the QRFH is a narrowing feed pattern beamwidth in the upper end of the frequency range, particularly in H-plane (perpendicular to the polarization vector). This reduces reflector illumination efficiency, and increases the cross-polarization, as the principal patterns become largely unequal to each other at the top of the band. A differential excitation can alleviate some of this by improving modal purity at the excitation point [11], [15]. To drastically improve the feed pattern beamwidth control, dielectric loads or lenses have been used [16]–[18]. Recently this was implemented in a 10:1 QRFH with a small low-loss and non-invasive polytetrafluoroethylene (PTFE) load resulting in a more stable H-plane [19]. In this paper, we take this concept further and introduce a novel QRFH with dielectric load covering 1–20 GHz with several scientific contributions:

- 1) Unprecedented 20:1 bandwidth, with beamwidth stability using a non-invasive, compact, and homogeneous dielectric insert at the QRFH center.
- 2) Two-piece manufacturing process of the dielectric to improve small-detail accuracy and access. Manufactured in space-grade polyimide with low out-gassing in vacuum.
- 3) Analytic-spline-hybrid (ASH) ridge profiles, implementing 3D-cubic splines to improve polarization efficiency and matching in the low frequencies.
- 4) Thermal and electrical analysis of aluminum alloy and dewar assembly for cryogenic installation and system noise temperature measurements on the ATA.

Section II of this paper focuses on the electromagnetic

modelling and optimization technique used. In Section III, details of the mechanical design and thermal analysis are presented to improve the community understanding of the fabrication process. Section IV details the predicted electromagnetic performance of the feed separate and on dish. In Section V, measured feed patterns are presented together with an assessment of material uncertainties in the complex dielectric permittivity. It is shown that the design allows for a variation in the relative permittivity while still performing well. With a simulated tolerance analysis we recreate the small deviation from nominal performance discovered in measurement. This analysis helps to set up a tolerance specification in future iterations. Section VI presents the system noise temperature measurements with the feed prototype installed on the ATA, and in Section VII the work is summarized with conclusions. The QRFH design presented in this paper is an excellent alternative to cover UHF to K-band with a single feed package for large arrays with constrained budgets.

## II. ELECTROMAGNETIC MODEL

The key design concepts introduced in this unique QRFH design are highlighted in this section together with the design parameters describing the model. At the end of this section the optimization procedure is described. The model was designed in CST Microwave Studios using a cubic 3D-spline curve function to define the top part of the ridge profile (Fig. 2a). In this paper, the notation of the profile shapes of horn wall, ridge, and dielectric are consistently expressed as  $x(z)$  where the  $x$ -coordinate is the radius or width with the  $z$ -coordinate length (optical axis) as the argument. For the upper part of the ridge profile that flares towards the horn aperture, five points describe the 3D-spline and are given as coordinates  $(x, y, z)$  relative to the origin located at the bottom center of the feed.

### A. Horn Profile

The circular-symmetric shape of the horn wall is modeled with two different analytic profiles [20] joined together at an inflection point, illustrated in Fig. 2a. The first horn profile,  $x_{h1}(z)$ , controls the shape in the vicinity of the excitation point allowing for a small bottom radius. This reduces the length of the coaxial hole in manufacture. The first horn profile is defined with a hyperbolic function:

$$x_{h1}(z) = \left| \sqrt{\frac{r_{h1}^2 + z^2(r_{h2}^2 - r_{h1}^2)}{L_{h1}^2}} \right|. \quad (1)$$

The second horn profile,  $x_{h2}(z)$ , controls the flaring of the horn towards the aperture and is defined with a power function:

$$x_{h2}(z) = r_{h2} + (r_{ha} - r_{h2}) \times \left( (1 - A_h) \frac{z}{L_{h2}} + A_h \left( \frac{z}{L_{h2}} \right)^{p_h} \right). \quad (2)$$

The inflection point between the profiles, and therefore also the starting point of  $x_{h2}(z)$ , is located in  $[L_{h1}, x_{h1}(L_{h1})]$ . The parameters and optimized values are found in Table I.

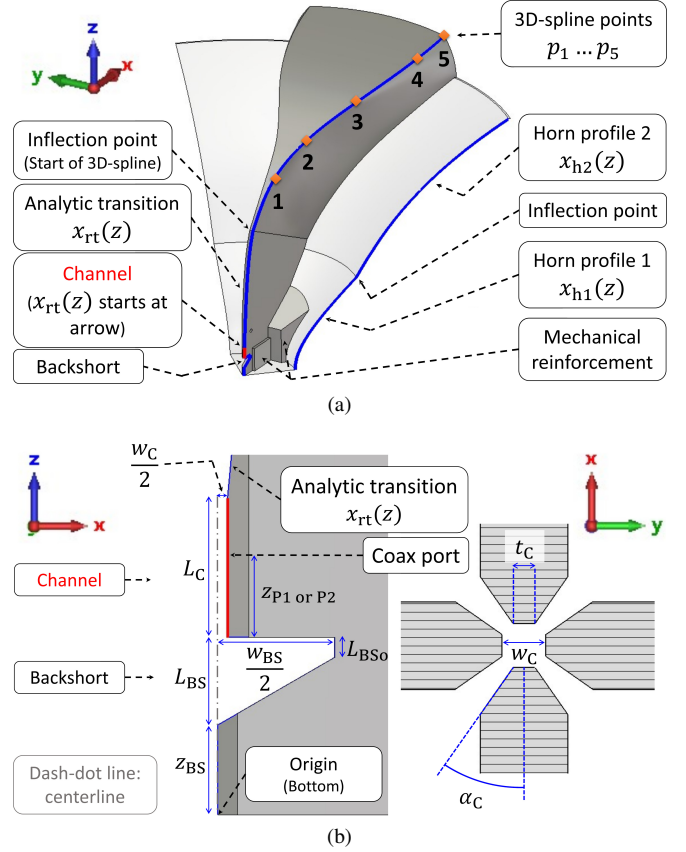


Fig. 2: QRFH quarter: (a) perspective view; (b) side view zoom-in of the channel and backshort (left), and top view cross-section of ridge-to-ridge separation (right).

TABLE I: Final parameters for horn wall profiles

Description	Notation	Value	Unit
Profile 1 radius	$r_{h1}$	28.0	mm
Profile 1 length	$L_{h1}$	48.6	mm
Profile 2 radius	$r_{h2}$	61.2	mm
Profile 2 length	$L_{h2}$	79.9	mm
Profile 2 linear ratio	$A_h$	0.42	unit-less
Profile 2 power exp.	$p_h$	2.6	unit-less
Horn aperture radius	$r_{ha}$	143	mm

### B. Ridge Profile and Backshort

The ridge profile is defined in multiple sections as an analytic-spline-hybrid (ASH) [21] to increase degrees of freedom for parts of the ridge while keeping parameter search space to a minimum during optimization. In Fig. 2 the different sections are highlighted. The different sections are described from top of the ridge to the bottom here:

1) *3D-spline Profile*: For the design presented in figure 10 of [19], the polarization efficiency is reduced at the low-frequency end. It has been shown previously that flaring the ridge thickness towards the aperture reduces certain unwanted higher-order modes [16]. In order to have more degrees of freedom to optimize radiation performance by the local flare control of the ridge, 3D-cubic spline profile for the upper section of the ridge was introduced in the present work. The

five coordinate points interpolated in the spline are illustrated in Fig. 2a and the optimized values are presented in Table II. The number of points is a trade-off between size of parameter search space and the degrees of freedom deemed necessary.

TABLE II: Final points for 3D-spline ridge

Notation	$(x, y, z)$
$p_1$	(27.5, 2.04, 98.1)
$p_2$	(49.5, 7.9, 113.6)
$p_3$	(80, 24.3, 130.7)
$p_4$	(128.6, 39.8, 146.7)
$p_5$	(144, 41.5, 150.4)

2) *Analytic transition*: Simulations showed that a planar ridge of 2 mm thickness around the point of excitation (coax) was required for good wideband matching. It was also desired with a planar ridge section at the center of the feed so that the dielectric, inserted between the ridges, can be designed with planar smooth slots for simplified manufacture and installation. Based on a large amount of simulations, there was no noticeable performance benefit from increasing the parameter search space and defining also the transition with cubic splines. Therefore, the planar analytic ridge transition was kept and its profile described by the power function:

$$x_{rt}(z) = x_{rt1} + (x_{rt2} - x_{rt1}) \times \left( (1 - A_{rt}) \frac{z}{L_{rt}} + A_{rt} \left( \frac{z}{L_{rt}} \right)^{p_{rt}} \right). \quad (3)$$

The parameters and optimized values for (3) are listed in Table III. Note that (3) is not defined with radii as it is not used for a circular-symmetric structure but rather as a contour that is thickened to create the planar base of the ridge with thickness  $t_{rt} = 2.0$  mm.

TABLE III: Final parameters for analytic ridge transition

Description	Notation	Value	Unit
Transition width 1	$x_{rt1}$	$w_C/2^*$	mm
Transition width 2	$x_{rt2}$	10.6	mm
Transition length	$L_{rt}$	62	mm
Transition linear ratio	$A_{rt}$	0.916	unit-less
Transition power exp.	$p_{rt}$	4.6	unit-less
Transition thickness	$t_{rt}$	2	mm

\* $w_C$  is the channel width, presented in Fig. 2b and Table IV

3) *Channel, backshort, and ridge separation*: The channel is defined as the straight and chamfered section where the ridge-faces are in closest proximity to each other and the excitation point is located for the two polarizations. On the left in Fig. 2b the channel is highlighted in red, and on the right side seen from the top in cross-section ridge-to-ridge (shown without coax for clarity). The width and length of the channel is defined with  $w_C$  and  $L_C$  respectively. The chamfered cut to create the flat face-tip of the channel is defined with thickness  $t_C$  and angle  $\alpha_C$ . The channel starts just above the backshort. The backshort cross-section is that of an isosceles triangle turned up-side-down with a small offset in the base-corners for machining purposes. On the left side of

Fig. 2b half of this triangle, corresponding to its cross-section in one ridge, is presented. This shape was proven less prone to sharp resonances in-band over the very wide frequency range compared to the traditional square shape. The backshort is parameterized in width  $w_{BS}$ , length  $L_{BS}$ , corner-offset  $L_{BSO}$ , and coordinate  $z_{BS}$  relative to the model origin (bottom). Final optimized values for these details are found in Table IV.

TABLE IV: Final parameters for backshort, channel, and ports

Description	Notation	Value	Unit
Channel width	$w_C$	1	mm
Channel length	$L_C$	7	mm
Channel face-tip thickness	$t_C$	0.5	mm
Channel chamfer angle	$\alpha_C$	35	deg
Backshort width	$w_{BS}$	11.8	mm
Backshort length	$L_{BS}$	4.4	mm
Backshort corner offset	$L_{BSO}$	1	mm
Backshort start	$z_{BS}$	4.5	mm
Port 1 relative to $L_{BS} + z_{BS}$	$z_{p1}$	1.20	mm
Port 2 relative to $L_{BS} + z_{BS}$	$z_{p2}$	1.96	mm

The location of the coaxial ports,  $z_{p1}$  and  $z_{p2}$ , are given in Table IV relative to the start of the channel (or end of backshort). Their individual offset was optimized for 45 dB isolation with launch-pin diameter of 0.020" (0.508 mm) which is a common standard for SMA connectors. Port 2 is offset +0.76 mm from port 1, which also is compensated for with the backshort length. For port 2 an additional +0.76 mm is added to  $L_{BS}$  and  $L_{BSO}$ , visualized in Fig. 6b and Fig. 6c.

### C. Dielectric Profile

In [19] a small, rotational-symmetric, PTFE insert was designed based on a simple cone-cylinder-cone structure with a small cylindrical extension from the bottom cone added for mechanical stability and locking mechanism. The small footprint of the dielectric and strong contact with the ridges has the potential to mitigate the risk of very large temperature gradients across the material [22]. The pointed top cone of the dielectric in [19] had a length of 2.5 mm or 1/3 of the cylindrical body diameter of 7.5 mm, which was straightforward to manufacture in a lathe. The dielectric presented in this paper is evolved from the same initial shape, but with design and material modifications to extend the frequency to 20 GHz. Through optimization it was found that the pointed top cone length now needs to be more than 5 times the cylindrical body diameter for the current design. To reduce the cost and complexity of machine turning such a structure with precision in polymer material, a constraint on the minimum radius was set to 0.75 mm. The top was also parameterized with a polynomial function to allow for a non-linear, more robust, transition from the thicker cylindrical body into the narrow top while keeping the parameter search space small:

$$x_d(z) = r_{dc} - (r_{dc} - r_{dt})(1 + p_{dt}) \times \left( 1 - p_{dt} \frac{z}{(1 + p_{dt})L_{dt}} \right) \left( \frac{z}{L_{dt}} \right)^{p_{dt}}. \quad (4)$$

The dielectric profile in (4) is illustrated in Fig. 3a as a split for visualization. The bottom cone has a small cylindrical



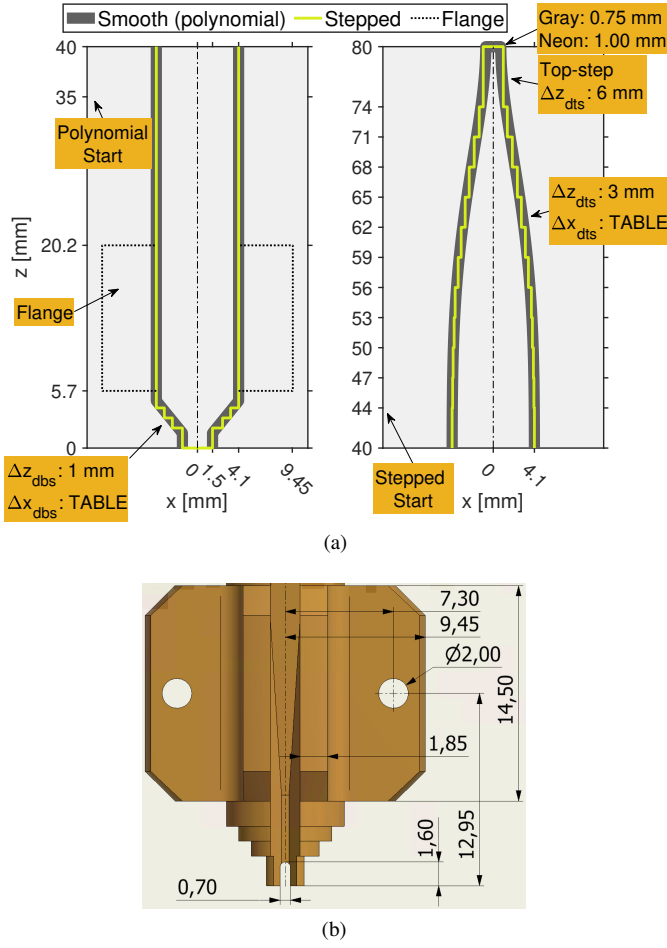


Fig. 3: (a) The dielectric smooth profile used for optimization (and first prototype) overlaid with the stepped profile used for final design.  $\Delta x_{dts}$  for the dielectric top steps and  $\Delta x_{dbs}$  for the bottom are presented in Table VI; (b) Mechanical dimensions in millimetre of flanges, and the slot for launch-pin (bottom).

extension of  $L_{dbe} = 2$  mm at the base. Above the bottom cone the cylindrical body extends to  $z = 35$  where it transitions into the polynomial top described by (4). In regard to its placement relative to the ridge the coordinate  $z = 0$  (bottom of dielectric) is located 1 mm above the junction between  $L_C$  and  $L_{BS}$  in Fig. 2b. The dielectric load measures 80 mm in length with a maximum diameter of the cylindrical part of 8.2 mm. The relative permittivity was modeled using CST's internal material function with a near-constant value over frequency and was found through optimization to ideally be  $\epsilon_r = 3.5$ . All the optimized parameter values for the dielectric are presented in Table V. Note the overlaid stepped profile in Fig. 3a which was introduced to simplify manufacturing of the final design and is further motivated in Section III-F. The step-sizes used for this profile are found in Table VI and Fig. 3a. In [19] the dielectric was prevented from sliding out when the feed is upside down by locking it to the backshort. To allow for a simpler insertion and extraction of the dielectric, the model presented here does not lock into the backshort and can be slid into place after the metallic parts are assembled.

TABLE V: Final parameters for the dielectric

Description	Notation	Value	Unit
Top radius	$r_{dt}$	0.75	mm
Top length	$L_{dt}$	45.0	mm
Polynomial power	$p_{dt}$	4.2	unit-less
Cylinder radius	$r_{dc}$	4.1	mm
Cylinder length	$L_{dc}$	30.3	mm
Bottom cone length	$L_{db}$	2.7	mm
Bottom cone radius	$r_{db}$	2.0	mm
Bottom cone cyl. ext.	$L_{dbe}$	2.0	mm
Relative permittivity	$\epsilon_r$	3.5	unit-less

TABLE VI:  $\Delta x$  for stepped profile top and bottom in Fig. 3a

$\Delta x_{dts}$ - top steps in millimeter
4.1, 4.05, 4.0, 3.9, 3.8, 3.5, 3.2, 2.8, 2.4, 1.9, 1.4, 1.0
$\Delta x_{dbs}$ - bottom steps in millimeter
4.1, 3.3, 2.5, 1.5

To prevent the dielectric from sliding out, small flanges with thru-holes were included as part of the structure, see Fig. 3b. The width (9.45 mm), length (14.5 mm), thickness (1.85 mm), and position of the flanges were found through simulation to not have an effect on performance. The corresponding hole in the ridge assumes threaded M2-grub screws (symmetric shape) to hold it in place. During optimization the grub screws were modeled as stainless steel 304 with magnetic properties which did not degrade performance, also confirmed with s-parameter measurement.

#### D. Optimization

The QRFH was optimized in multiple steps, with different parameter search space and size targeting different parts of the feed throughout the process. The performance across the UWB frequency range is affected by different features of the feed. For the feed radiation pattern, the combination of horn wall and ridges dominates the first octave and slightly above in frequency (1–3 GHz). Beyond 3 GHz, the dielectric load has a very strong influence on the pattern performance. For the cut-off and impedance match the horn size and ridge-to-ridge spacing is very important across the band with a strong effect on the cut-off shape from the dielectric. These results are quantified further in Section IV. Due to this complex relationship the optimization procedure can best be summarized in three significant milestones:

- 1) Finding the horn, ridge and dielectric baseline shapes using planar ridges. In this step the relative permittivity  $\epsilon_r$  was varied between 2 and 5, converging to 3.5. Search space includes all parts of the model in a global search.
- 2) Finding the ridge's flared upper shape with 3D-spline. Search space includes horn and ridge, dielectric is fixed.
- 3) Final and more local search including all parameters.

In all iterations the entire frequency range 1–20 GHz was evaluated, with a frequency step of 0.5 GHz for the pattern evaluation. The goal function evaluates for two properties:

- 1) **Aperture efficiency** which is the ratio  $\eta_a = A_{\text{eff}}/(\eta_{\text{rad}} A_{\text{phy}})$  characterizing how large the effective

area,  $A_{\text{eff}}$ , is from feed illumination of the physical reflector area  $A_{\text{phy}}$ . The radiation efficiency (losses) is denoted here with  $\eta_{\text{rad}}$ , and assumed to be unity during optimization. The  $\eta_a$  can be calculated from the co-polar gain ( $\eta_{\text{rad}} = 1$ ) resulting from the feed-to-reflector simulation, or by the product of its sub-efficiencies [23], [24] based on the feed pattern  $\eta_a = \eta_{\text{ill}}\eta_{\text{sp}}\eta_{\text{BOR1}}\eta_{\text{pol}}\eta_{\text{ph}}$ . Here  $\eta_{\text{ill}}$  is the illumination efficiency;  $\eta_{\text{sp}}$  is the spill-over efficiency;  $\eta_{\text{BOR1}}$  is the BOR1 (azimuth mode) efficiency;  $\eta_{\text{pol}}$  is the polarization efficiency in the 45 degree plane; and  $\eta_{\text{ph}}$  is the phase efficiency relating to the feed phase center location relative to the reflector focus. Due to the very large frequency range, the calculation of  $\eta_a$  from the feed patterns is preferred since it reduces iteration time and allows for finer frequency steps.

- 2) **Input reflection coefficient** that characterizes the feed impedance match to 50- $\Omega$  single-ended ports.

The feed was optimized with goals of  $\eta_a > 60\%$  in a half-subtended angle of  $60^\circ$ , and input reflection  $S_{11} < -10$  dB across the band, with penalties upon deviation from these goals. The maximum number of parameters in the search space for the electromagnetic design was 45. The simulation and goal function evaluation were done through a MATLAB/CST-pipeline. For global search the particle swarm optimization (PSO) algorithm was used. Additional smaller and local optimizations on the following parameters were performed to have a practical mechanical model: the relative location between the ports to improve isolation (minimize  $S_{21}$ ), the mechanical reinforcement of the ridges around the coaxial hole, and the flanges of the dielectric. The later two were designed so to not deteriorate optimized performance. These features are described in Section III and are included in the simulated (and measured) results presented in this paper. Normally it is good practice to optimize feeds for maximum sensitivity rather than  $\eta_a$ . Sensitivity can be expressed as  $T_{\text{sys}}/\eta_a$  where  $T_{\text{sys}}$  is the system noise temperature with contributions from sky, spill-over and receiver where the later two are specific to reflector geometry and LNA. During the design-phase, no valid LNA covering the full frequency range has been identified, and the reflector geometry was kept generic for multiple applications. In Section IV the feed is evaluated for performance in several geometries to show the versatility in application. It should be noted that the prototype feed's diameter in the present work has been constrained in optimization to fit inside the vacuum dome of the existing ATA cryostat. The glass dome has an inner diameter of 290 mm. The length of the feed (without the interface-specific bottom flange) is 170 mm.

### III. MECHANICAL DESIGN

#### A. Aluminum alloy

Aluminum is a common material choice for machined manufacture of QRFHs with frequency ranges in the order of gigahertz. It is a lightweight, machinable and cost-effective material with good electrical and thermal conductivity. It also presents low emissivity with careful machining for use in cryogenic dewars. The machinability of the different alloys varies, with Al-5083 being a good choice for high-tolerance

and rapid manufacture. However, typically Al-6082 or Al-6061 are chosen for their higher conductivity both electrically (reduced loss) and thermally (reduced heat load). Due to the QRFH's cryogenic application in this work, the impact on the cryocooler heat load and also ohmic loss contribution to  $T_{\text{sys}}$  has been modeled for different choice of aluminum alloys.

#### B. Thermal Analysis

The CAD model of the feed was reconstructed and thermally analyzed using ESATAN-TMS 2021 [25], a European space industry standard thermal analysis software. The cryogenic dewar in which the QRFH was tested was also included in the thermal model, further detailed in Section VI. In Fig. 18a, the dewar is shown with the most prominent features: glass dome (borosilicate glass); QRFH with bottom flange (al-5083 or al-6061) connected through an adapter (al-6061) to the plate which is connected to the cold head with thermal straps (all three, OHFC copper). The copper plate is attached to the baseplate (stainless steel 304) with small stand offs (Ti-6Al-4V). The thermal model is a mathematical representation of the heat flows within this assembly. The assembly is discretized into nodes, which are areas considered to be isothermal and are assumed to have their mass lumped at the center of the node. Finite difference method assumptions are then used to solve the partial differential equations of the heat flows between the nodes for the radiative and conductive heat transfer. The total model is comprised of 536 nodes; one of which represents the radiative environment held as a boundary at 298 K, and one of which represents the cryocooler held as a boundary at 85 K. The modeling of the cryocooler inner workings is not considered. Only the metallic part of the feed is included specifically targeting the choice of aluminum alloy. The dielectric load, coaxial feeding, nuts and bolts are not considered in this analysis, as they are independent of the aluminum alloy, and will instead be evaluated from long-term temperature monitoring of the receiver. The material properties assumed in these simulations are presented in Table VII for  $T_{\text{phy}} = 80$  K (varies with  $T_{\text{phy}}$  in simulation). Of particular interest is the difference in thermal conductivity between the two aluminum alloys. The temperature map of the results for both materials are shown overlayed on the ESATAN-TMS geometry of the feed in Fig. 4, with key numbers presented in Table VIII. It can be seen from these results that the delta effect is negligible, and that for both materials the heat load is within the cryocoolers available heat lift (19 W at 85 K). As expected, the results show that the lower conductivity of the Al-5083 causes an increase in both the feed overall temperature, and the temperature gradient through it. However, the increase is not to a level that it has an adverse effect on the thermal load, and it does not represent the largest temperature delta in the assembly. The greatest contributors to the increase in temperature through the assembly remain the thermal strap; with a physical temperature delta across it of  $\Delta T_{\text{phy}} \approx 7$  K, and the aluminum adapter; with  $\Delta T_{\text{phy}} \approx 5$  K. From a thermal perspective it is therefore acceptable to use either Al-6061 or Al-5083. It should also be noted that the planar bottom flange attaching to the QRFH quarters was in prototyping made from

Al-6082 which has similar properties as Al-6061. In thermal simulation it is assigned the same alloy used for the feed in each case.

TABLE VII: Thermal material properties for feed and cryostat assembly at  $T_{\text{phy}} = 80 \text{ K}$  ([26]–[29]). Nomenclature: Emissivity,  $\varepsilon$ ; Transmissivity,  $\tau$ ; Thermal Conductivity,  $\kappa$ ; Specific heat,  $c_p$ ; Material density,  $\rho$ . No solar impingement assumed.

	Unit	Stainless Steel 304	OFHC Copper	Borosilicate Glass	Al-6061*	Al-5083*	Ti-6Al-4V
$\varepsilon$	unit-less	0.14	0.1	-	0.05	0.05	-
$\tau$	unit-less	-	-	0.9	-	-	-
$\kappa$	[W/mK]	8.1	500.3	1.14	85.6	56.8	3.5
$c_p$	[J/KgK]	215.3	205.1	830	368.7	368.7	-
$\rho$	[Kg/m <sup>3</sup> ]	8000	8960	2230	2700	2700	-

\*The emissivity numbers assume Surtec 650 coated aluminum for consistent lifetime performance [30]. For the manufactured QRFH prototype described in this paper, coating has not been applied because of time constraints.

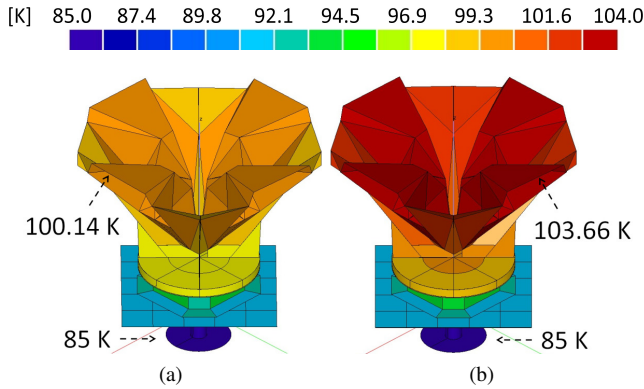


Fig. 4: Simulated thermal map for alloys (a) Al-6061; (b) Al-5083; with cold head at 85 K and environment at 298 K.

TABLE VIII: Details from thermal results presented in Fig. 4

	Al-6061	Al-5083	$\Delta$	Unit
Cold head $T_{\text{phy}}$	85.00	85.00	-	K
Cold head thermal load	10.34	10.32	-0.02	W
QRFH max. $T_{\text{phy}}$	100.14	103.66	+3.52	K
QRFH min. $T_{\text{phy}}$	96.90	98.98	+2.08	K
QRFH gradient $T_{\text{phy}}$	3.24	4.68	+1.44	K

### C. Ohmic Loss

To model the impact of the ohmic (resistive) losses for different aluminum alloy, simulation of the QRFH model in CST MWS is performed to calculate the relative difference in radiation efficiency. The QRFH model is here simulated without dielectric, and a smooth material surface. Due to the inconsistency in available data of electrical conductivity (or resistivity) with temperature dependence for different aluminum alloys, the Wiedemann-Franz law was used to approximate these numbers. This law relates the electrical conductivity  $\sigma$  with the thermal conductivity  $\kappa$  of metals through the Lorenz number  $\mathcal{L}$  and  $T_{\text{phy}}$  according to  $\kappa/\sigma = \mathcal{L}T_{\text{phy}}$ . The Lorenz number has a general value of  $\mathcal{L} = 2.45 \cdot 10^{-8} [\text{W}\Omega\text{K}^{-2}]$ ,

although it varies with temperature and metal ([31], p. 144). The variation of  $\mathcal{L}$  is in the present work assumed to be small enough between different aluminum alloys and temperatures so that it can be ignored, and that specific Lorenz number for aluminum will only cause an offset from the absolute value in electrical conductivity. Using this law, thermal conductivity for Al-5083 and Al-6061 ([27]) at  $T_{\text{phy}} = 4, 80$ , and 298 K are converted to electrical conductivity, presented in Table IX. For simulations at 20 GHz, the increase to the overall noise temperature is  $\Delta T_{\text{loss}} = 0.3 \text{ K}$  at  $T_{\text{phy}} = 80 \text{ K}$  when using Al-5083 compared to Al-6061 (Table IX). Even at  $T_{\text{phy}} = 298 \text{ K}$  the  $\Delta T_{\text{loss}}$  is less than 1 K and is therefore a non-deciding factor for the choice of aluminum in this design.

TABLE IX: Thermal ( $\kappa$ , [W/mK]) and electrical ( $\sigma$ ,  $10^7 [\text{S/m}]$ ) conductivity for Al-6061 vs Al-5083 over  $T_{\text{phy}}$ . Simulated loss increase ( $\Delta T_{\text{loss}}$ ) from using Al-5083 is presented at 20 GHz

	Al-6061		Al-5083		$\Delta T_{\text{loss}}$ at 20 GHz
	$\kappa$	$\sigma$	$\kappa$	$\sigma$	
$T_{\text{phy}} = 4 \text{ K}$	5.0	5.1	5.0	5.1	+0.0 K
$T_{\text{phy}} = 80 \text{ K}$	85.6	4.4	56.8	2.9	+0.3 K
$T_{\text{phy}} = 298 \text{ K}$	155	2.1	120	1.6	+0.9 K

### D. Manufacture - Quarters



Fig. 5: Manufactured quarters and bottom plate.

The feed horn wall and ridges were manufactured as single-piece quarters with high precision of the ridge center-line and quarter side-to-side perpendicularity. The quarter structure enables excellent ridge-to-ridge alignment with a reduced number of thermal interfaces between parts. The quarters' basic shape were machined in Al-5083 as a two-cut pass with a computer numerically controlled (CNC) wire cutting electrical discharge machine (EDM). The remaining material was then removed with a 5-axis CNC mill, i.e. the horn walls, ridge-sides and weight-reducing pockets. Care was taken to retain the form of the ridges throughout and particularly where they narrow down towards the base. The wire cutting process as a two-cut pass is a good compromise between cost and smoothness with a geometric form near perfect. The smoothness is increased by multiple passes but at significant cost, and deemed not needed for this application from the manufacturers experience. A ball-nosed mill would have produced a more mirror-like surface but also a waviness at the surface dependent on the overlap of each cut also pertaining to the time and cost.

Due to the cutting fluids used in typical machining process, the quarters and bottom flange were cleaned from residue in a three-step process with soap-water, acetone and isopropanol including ultrasonic cleaning. This improves electrical contact and thermal surface-to-surface transfer after assembly together with vacuum grease applied between the quarters and the bottom flange to fill micro-creases. The quarters are bolted (M5) together through the flanges running along their perpendicular sides. Holes are separated by 1.5 cm along the flange corresponding to  $\lambda$  at 20 GHz rather than the sometimes preferred  $\lambda/2$  or  $\lambda/4$  separation. It was deemed that a large bolt dimension, rather than multiple tightly spaced smaller bolts, would give a sufficient electrical and thermal connection due to the high precision of the machined surfaces. Extending from the flanges are also additional flat surfaces (see bottom right in Fig. 18a) where extra thermal straps (copper braids) can be attached if thermal transfer from quarters down to the cold head is not sufficient. Each quarter side has two spatially separated dowels, one at the top and one at the bottom, for precision alignment side-to-side. The bottom flange was manufactured in Al-6082 in a 3-axis CNC mill and is bolted through threaded blind-holes on the underside of the quarters (M4). The bottom flange is customized for the specific adapter used (Fig. 18a) and can be modified for a different interface. Due to the vacuum application, vented bolts were used in the blind-holes to mitigate the risk of leakage from trapped air over time. To retain strong contact over multiple cryogenic cycles, all bolted connections have beryllium-copper spring washers.

#### E. Excitation - press-fit termination in blind-hole

The QRFH has two single-ended 50- $\Omega$  output ports with standard female 3.5 mm SMA connectors with PTFE dielectric (Southwest: 214-512SF) that accepts a pin diameter of 0.020 inch (0.508 mm), see Fig. 6d. They are specified from DC to 27 GHz and connector back-to-back measurements has a maximum 25.5 dB return loss per connector over 1–20 GHz. The coaxial outer conductor is a two-step hole through the ridge with total length of 27.5 mm (Fig. 6e). The hole has a 18.5 mm long section with a diameter of 1.7 mm where the pin is supported by dielectric (50- $\Omega$  dimensions). This section improves concentric alignment during insertion as well as mitigating any risk of a short circuit as the pin travels through the 9 mm long, 1.1 mm diameter, air-filled section (Fig. 6a). The 1.7 mm diameter also reduces difficulty to achieve concentricity tolerances when machining the hole compared to an all air-filled hole with 1.1 mm diameter through the whole ridge. The air-filled section's diameter was optimized for best impedance transitioning from the 1.7 mm dielectric-filled hole. The result is that a diameter of 1.1 mm provides better match than a diameter of 1.2 mm that corresponds to a 50- $\Omega$  air-filled coax with pin diameter of 0.508 mm. The ridge is locally reinforced around the coaxial hole and the horn wall where the SMA is connected, seen in Fig. 16a. These features did not impact the optimized performance. The gold-plated launch-pin is terminated in the opposing ridge by press-fit into a blind-hole (Fig. 6d). The blind-hole was

machined with a snug 0.5 mm diameter and  $\sim 3$  mm depth, see the left-most dimensions in Fig. 6e. With this technique, and the dielectric support, the prepared SMA package (Fig. 6d) conveniently slides into stable contact with the opposing ridge without the need for complex threaded or soldered solutions [10] that can lead to uncontrolled plane of termination and concentric misalignment. The gold layer of the pin ensures a good contact after insertion, and the stainless steel body mitigates the risk of reduced contact when cooled as the linear expansion coefficient is lower than for surrounding aluminum [27]. The total length of the pin is 34 mm, from bottom of the SMA socket to bottom of the ridge blind-hole, and the end of the pin has a slightly pointed tip for guiding. The press-fit technique has previously been shown successful up to 50 GHz in a QRFH made from brass [14].

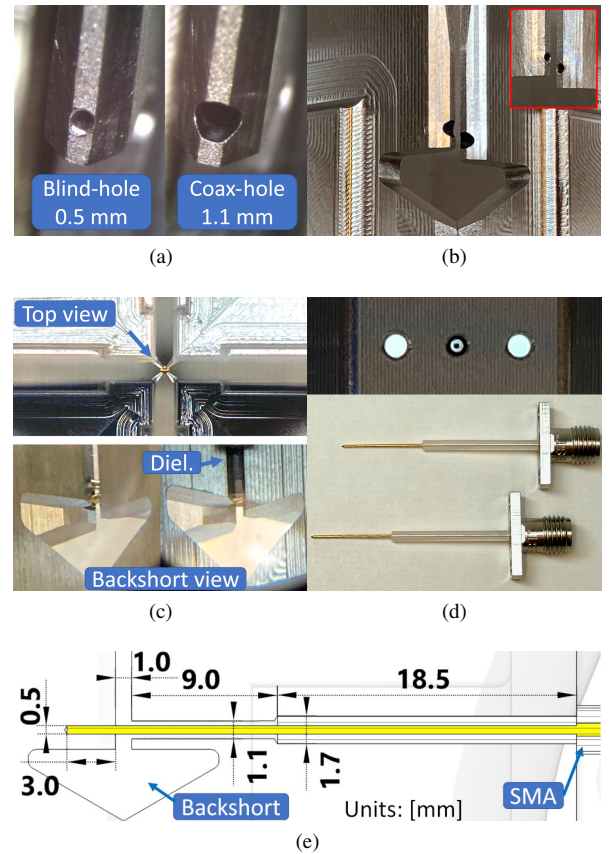


Fig. 6: (a) Holes on ridge face; (b) Port offset; (c) Launch-pins installed, without and with dielectric load installed; (d) Alignment of ridges with blind-hole seen through coax-hole (top), SMA with launch-pins (bot); (e) Cross-section of excitation.

#### F. Dielectric Load

To select a suitable dielectric candidate material, a general assessment of available data was done, see Table X. Data from supplier data sheets is often a single point value at 1 MHz or 1 kHz for the relative permittivity ( $\epsilon_r$ ) and loss tangent ( $\tan\delta$ ). This introduces an uncertainty in the final design parameters for optimal electromagnetic performance



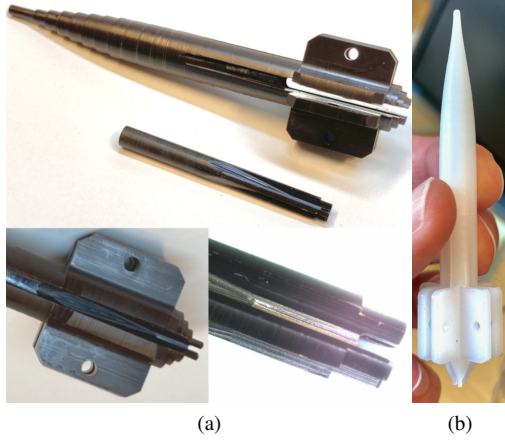


Fig. 7: Manufacture: (a) Final dielectric in polyimide with step-profile, as a two-piece part joined by insertion; (b) First dielectric as one piece in POM with smooth profile.

TABLE X: Materials with relative permittivity near  $\epsilon_r = 3.5$

Material properties	f[GHz]	$\epsilon_r$	$\tan\delta \cdot 10^{-3}$	Ref.
<b>Polyimide (PI, unfilled)</b>				
- Ensinger TECASINT 2011	0.0001	3.4	1.0*	[32]
- DuPont Vespel SP1	0.001	3.55	3.4	[33]
Polyphenylene Ether (PPE)				
- PREPERM PPE350	22	3.5	2.4	[34]
Polyoxymethylene (POM)	10	3.6	30	[35]

\*From the similar stock TECASINT 4011 datasheet

over the frequency range of interest which is addressed further in Section V-2. The dielectric load was manufactured by CNC machining using a mix of dry (air) and wet (isopropanol) coolant. The basic outer shape (without slots and holes) is a circular symmetric form that can be manufactured with a lathe. To test the concept and improve the design before final manufacture, a first prototype was made out of opaque polyoxymethylene (POM, typically known by brand name Delrin) which is a common, low-cost, engineering thermoplastic used in many applications for high-precision structures. The relative permittivity is varying by brand and has a loss tangent far too high for the final application, see Table X. This prototype was CNC-machined with a lathe in one piece to achieve the smooth polynomial top in (4) and then milled to make the flanges and the slots for launch-pins and ridges (Fig. 7b). From this model it was concluded that the top diameter, previously constrained to 1.5 mm, was still slightly too small to easily be manufactured. It was also concluded that the smallest details in the slots for the ridges were difficult to machine with the whole dielectric load being one piece. Both challenges were addressed to simplify manufacture in the final design. The first challenge was addressed by fitting a stepped profile to overlay the polynomial top profile and the conical bottom, see Fig 3a. Once transferred into a stepped profile the top diameter was increased to 2.00 mm improving machinability without significantly altering performance. The stepped profile also allows for machining in a manual precision-lathe as the cross-section only has right angles (Fig 3a). The second challenge was addressed by splitting the part manufacture into two pieces

that later are joined through simple press-fit insertion of the inner piece into the outer piece with tolerances for a snug fit, see Fig. 7a. The inner piece has a maximum diameter of 3.7 mm, and a total length of 37.0 mm. The 2 mm cylindrical extension at the bottom has milled slots for the launch-pins to pass through, see bottom right in Fig. 7a and Fig. 3b. The corresponding 3.7 mm diameter hole in the outer piece is 35 mm deep measured from the bottom. The outer piece has a length of 78 mm, resulting in the total part length of 80 mm when the two pieces are joined. This way of manufacture allows for a more controlled milling of the small details in the ridge and launch-pin slots that measures 0.5 mm (channel face-tip thickness  $t_c$ ) at its narrowest pass (Fig. 7a). The material choice for the final dielectric design was *unfilled polyimide* (PI), not to be confused with polyamide or Nylon. The specific type of polyimide used here was TECASINT 2011 [32] which is designated with low moisture absorption, high toughness and machinability, and therefore commonly used in space applications. According to the supplier, testing that comply with European Space Agency (ESA) rigid standards indicate that no condensable impurities are found in TECASINT materials [36]. Therefore, it is a good choice for vacuum applications such as a cryogenic dewar that require low outgassing. It is specified with relative permittivity of  $\epsilon_r = 3.4$  at 0.1 MHz in room temperature, which is near the 3.5 modeled for the feed across 1–20 GHz. The data sheet for TECASINT 2011-grade does not have a specified loss tangent, but the closely related 4011-grade is specified with  $\tan\delta = 10^{-3}$ . A sample brick with dimensions 61.15x5.45x21.55 mm of the material was tested with submersion into liquid nitrogen (77 K) until temperature equilibrium was reached. Although difficult, attempts to measure the dimensions (digital  $\pm 0.03$  mm tolerance caliper) of the cooled sample were made. Only for the longest dimension was a noticeable and repeatable difference between warm and cold measurements found. The shrinkage was measured to 0.45 mm over the original length of 61.15 mm which corresponds to 0.7%. With the final dielectric load design having a total length of 80 mm, a 0.7% shrinkage is 0.5 mm. To apply a margin, a uniform 1.25% shrinkage of the dielectric was simulated and show only a small effect on performance with 0.5% lower  $\eta_a$ . The shrinkage corresponds to 1 mm of reduction of the dielectric length, and 0.1 mm of diameter reduction. The simulation assumes a uniform shrinkage, and no skewing due to the homogeneous material, compact and symmetric footprint, and fixation between ridges. Attempts were made to break the cooled sample by bending it with hand-strength without success. The only successful technique was fastening the sample in a bench vice and striking it repeatedly with significant force from a hammer. This strengthens the notion of the material indeed being suitable for cryogenic environment.

#### IV. ELECTROMAGNETIC PERFORMANCE

##### A. S-parameters

In Fig. 8 the simulated and measured s-parameters of the feed without and with dielectric are presented with mostly good agreement across the band. The s-parameters were measured with a calibrated Agilent E8362C PNA specified over



0.01–20 GHz. The de-embedded reference plane in measurement is the SMA connector interface of the QRFH. Measured band-average values of the input reflection is  $S_{11} = -13.6$  dB (Sim:  $-13.9$  dB) and  $S_{22} = -16.7$  dB (Sim:  $-17.8$  dB) for respective port with the dielectric installed. The importance of the dielectric in this design for a sharp low-frequency cut-off is clearly seen in Fig. 8 where measured  $S_{11}$  averaged over 1–2 GHz is  $-4.2$  dB and  $-11.6$  dB without and with the dielectric installed respectively. The port-to-port isolation band-average is  $S_{12} = S_{21} = -41.5$  dB (Sim:  $-48.7$  dB) with the dielectric installed. Measured peak  $S_{11}$  mid-band is  $-7.4$  dB and due to the relative permittivity of the manufactured dielectric load material further analyzed in Section V-2.

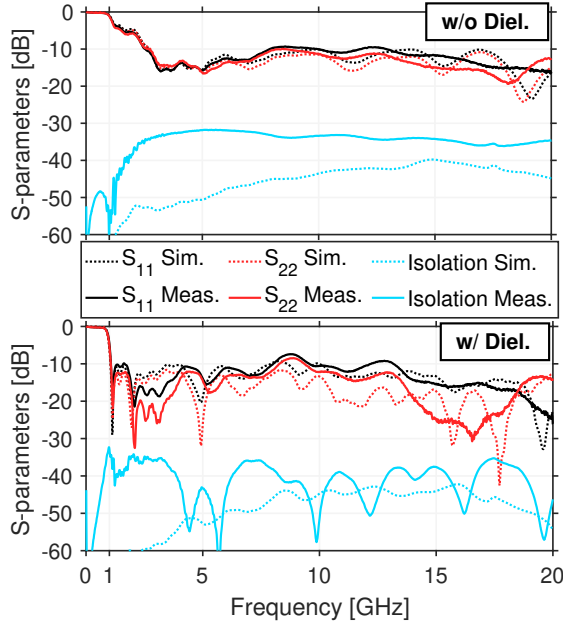


Fig. 8: S-parameters simulated (dotted) and measured (solid).

### B. Aperture efficiency and cross-polarization

The feed is predicted to nominally have a band-average aperture efficiency of  $\eta_a = 62\%$  in an unshaped reflector with half-subtended angle  $\theta_e = 60^\circ$ . The phase center to maximize  $\eta_a$  over the band is calculated to be 53 mm inside from the circular horn wall aperture. In Table XI the band-averages of the sub-efficiencies to  $\eta_a$  are presented without and with dielectric showing the importance of the dielectric to the design performance. A wide H-plane pattern across the upper frequency range, results in the principal patterns being more similar and an improved cross-polarization. The illumination efficiency,  $\eta_{ill}$ , is 18% higher with dielectric while the azimuth mode (BOR1) efficiency,  $\eta_{BOR1}$  is 7% higher meaning the dielectric contributes to power in the first order azimuth mode [37]. The polarization efficiency measuring the co-polar BOR1 power in the 45-degree plane to the total BOR1 power shows an efficiency 12% higher with dielectric. The low-frequency polarization efficiency presented in Fig. 9 is considerably improved compared to the design presented in figure 10 of [19]. This is largely due to the 3D-spline-defined

section of the ridges introduced in the present work. The cross-polarization ( $|XPD|$ ) is presented in Fig. 10. The band-average is 6.6 dB (6.8 dB) without dielectric and 9.1 dB (10.4 dB) with dielectric, where values in parenthesis are nominal simulated. The deviation from simulated with dielectric inserted is related to the  $\epsilon_r$  of the specific brand of material used for prototyping, further discussed in Section V-2.

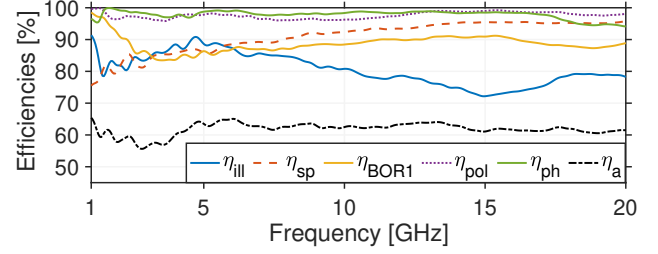


Fig. 9: QRFH aperture efficiency,  $\eta_a$ , and sub-efficiencies in unshaped and unshielded reflector with half-subtended angle  $60^\circ$  with the dielectric installed. Frequency step: 50 MHz.

TABLE XI: Band-average efficiencies over 1–20 GHz for QRFH in half-subtended angle  $60^\circ$  without and with dielectric

	$\eta_{ill}$	$\eta_{sp}$	$\eta_{BOR1}$	$\eta_{pol}$	$\eta_{ph}$	$\eta_a$
w/o Diel. [%]	63	93	82	86	90	38
w/ Diel. [%]	81	91	89	98	98	62

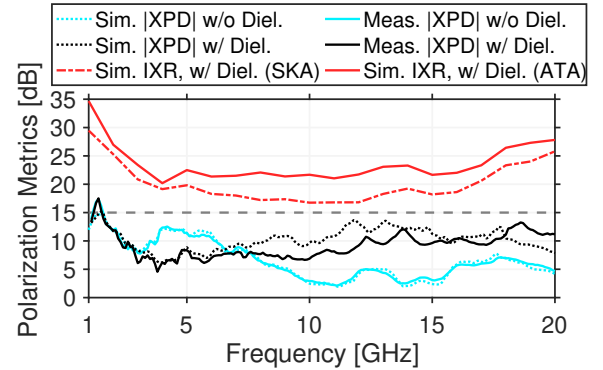


Fig. 10: Cross-polarization ( $|XPD|$ ) for the QRFH stand-alone and IXR in the unshaped ATA and shaped SKA dish.

### C. Unshaped and shaped reflector

The first prototype of the 1–20 GHz QRFH has been installed on one of the offset Gregorian reflectors of the ATA at the Hat Creek Observatory, CA, USA. The ATA reflector optics have a diameter of  $D = 6.09$  m and are designed with a half-subtended angle of  $\theta_e = 42^\circ$  [3]. The novel design of the hydroformed antennas include a spill-over rim on both main and sub-reflector and a shroud between them mitigating the dish-to-ground exposure, see Fig 11a. This allows for an increased over-illumination of the sub-reflector without a severe spill-over penalty. The QRFH was optimized for a half-subtended angle of  $\theta_e = 60^\circ$ , but is predicted to perform well in the smaller angle of the ATA due to the spill-over

protection. In Fig. 11b fullwave (FW) simulations over 1–15 GHz, and physical optics with physical theory of diffraction (PO-PTD) simulations over 1–20 GHz are presented. The PO-PTD simulations show a band-average (1–20 GHz) aperture efficiency of 53.4% for the QRFH installed on the ATA. Despite being an offset geometry, in PO-PTD simulations a small self-blockage ( $\sim 3\%$ ) is included from the sub-reflector covering the main-reflector with an estimated area of  $A_b = 0.43 \text{ m}^2$ . The fullwave simulation confirms that no interfering near-field effects between shroud and feed exists for illumination. Due to limited computer resources the fullwave simulations only cover 1–15 GHz. The large reduction of spillover temperature,  $T_{\text{spill}}$ , from the shroud is clearly seen in Fig. 11c. Band-average (1–15 GHz) spillover is reduced to a few Kelvin for the telescope pointing over a wide range of zenith angles,  $\theta_{\text{za}}$ . The antenna and spill-over noise temperature is calculated with a fullsphere integration of the power pattern and brightness temperature product. The brightness temperature is taken from the SKA-model [38], using 'Model 3' detailed in [39], p.1565. The QRFH was also simulated in the shaped SKA-dish with  $\theta_c = 58^\circ$  using PO-PTD. The aperture efficiency band-average is 72% which is 10% higher than in the unshaped generic reflector in Fig. 9 with similar half-subtended angle. This is due to the shaping of the SKA-dish. A simulated estimate of the receiving sensitivity for the QRFH in the ATA and SKA dish is presented in Fig. 11c. The sensitivity is presented normalized as  $T_{\text{sys}}/\eta_a$  (lower is better) for comparison without reflector size dependence. In this comparison, the modeled receiver noise contributions to  $T_{\text{sys}}$  is assumed to be the same as introduced in Section VI. Supporting struts and surface roughness are not included in these simulations. Sensitivity results show that for shielded reflector systems, which are implemented in all the previously mentioned large arrays [3], [40], [41], this feed presents an interesting UWB solution. As an example, the feed covers the SKA bands 2, 3, 4, and 5a/5b (frequency range: 1–15.4 GHz [42]) as a low-cost solution using one feed and needing only two LNAs compared to multiple octave packages with two LNAs each. There is no doubt that the *sensitivity per hertz* for an optimized octave system would be higher, but without the benefit of continuous available bandwidth from UHF to K-band. The competitiveness of such a system could be increased by improving the LNA performance to the full frequency range of the feed. The intrinsic cross-polarization (IXR) models the feed's polarization purity calculated on reflector independently of the coordinate system chosen [43]. It is retrieved from the maximum and minimum amplitude gain of the reflector beam pattern's Jones-matrix produced in simulation. In Fig. 10 it is seen that the QRFH presented in this paper fulfills the limit  $\text{IXR} > 15 \text{ dB}$  within half-power beamwidth (HPBW) set for the SKA. The IXR for both ATA and SKA dish are calculated from PO-PTD simulations.

## V. FEED PATTERN MEASUREMENT - ANECHOIC CHAMBER

The QRFH feed radiation patterns were measured in an anechoic spherical-nearfield/farfield chamber specified from 0.7 GHz and upwards. The chamber is equipped with oc-

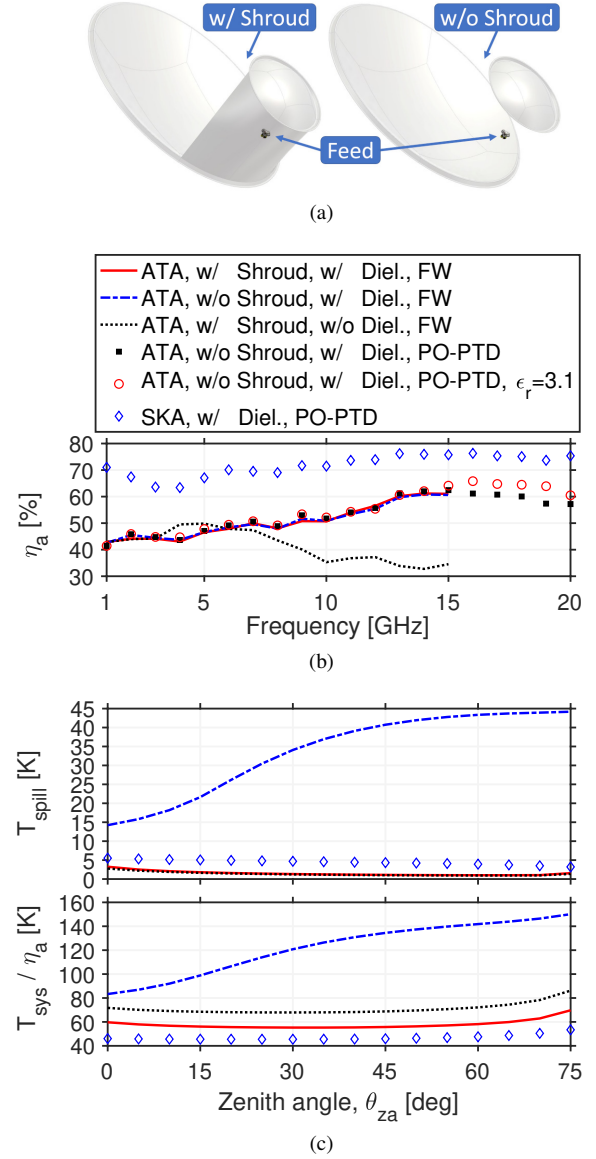


Fig. 11: (a) The ATA shroud; Simulated: (b)  $\eta_a$  over frequency; (c) band-average  $T_{\text{spill}}$  and sensitivity ( $T_{\text{sys}}/\eta_a$ ) over  $\theta_{\text{za}}$ .

tave probes for the standard waveguide bands and an additional wideband open boundary QRFH probe (ETS-Lindgren's Model3164-05) over 2–18 GHz to reduce the total number of probes. To center probe-to-DUT alignment, a sweep for minimum cross-pol defined the offset position used for each alignment. For the smallest wavelength, 1.5 cm at 20 GHz, the minimum distance at which the DUT is located in classic farfield is  $2D_s^2/\lambda = 2 \cdot 0.32^2/0.015 \approx 13.65 \text{ m}$  approximated by a sphere of diameter  $D_s = 32 \text{ cm}$  enclosing the device. This is more than double the length of the chamber, and therefore not possible. Due to the fact that QRFHs are sized on the order of its lowest frequency, spherical nearfield-to-farfield measurements over 20:1 bandwidth are extremely time consuming with the angular step size needed to sample the spherical grid decreasing with increasing frequency and antenna size. However, good approximations of a reduced farfield limit for measurement in small anechoic chambers

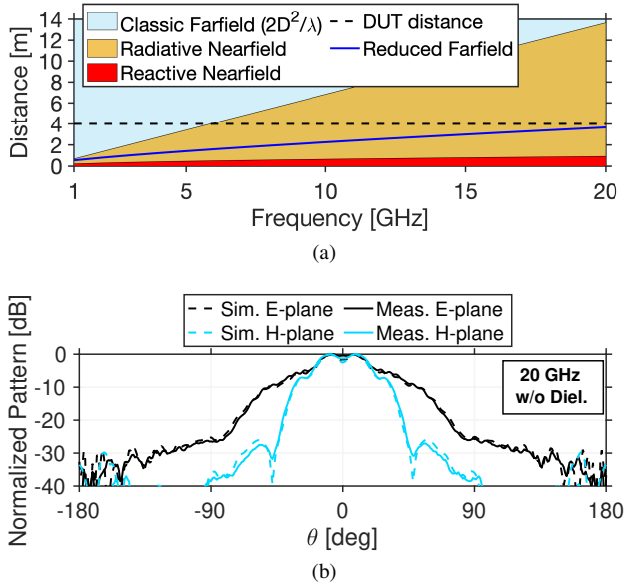


Fig. 12: (a) DUT distance (aperture-to-aperture) during pattern measurement in relation to field regions; (b) Simulated and measured pattern at 20 GHz at reduced farfield distance [44].

have been investigated to characterize 5G antennas [44]. This method is based on spherical wave expansion, assuming design for wideband with relatively high gain and an approximate error expected within 0.5 dB. The reduced farfield distance, from equation 2 in [44], for a sphere of  $D_s = 32$  cm is plotted against the classic limits of reactive and radiative nearfield, as well as the classic farfield, in Fig. 12a. The reduced farfield distance is located outside what is classic reactive nearfield with a margin. Using the reduced farfield limit, the distance was set to 4 m between probe and DUT aperture in the QRFH feed pattern measurements. With classic farfield this distance would limit measurements to 6 GHz. In Fig. 12b good agreement is presented for the normalized co-polar farfield pattern, measured at 4 m distance without dielectric, at the QRFH's highest operational frequency of 20 GHz. This indicates the reduced farfield is a good approximation to simplify UWB antenna measurement, reducing both cost and time while allowing for the use of smaller anechoic chambers. All feed patterns in this paper are given in linear co- or cross-polarization as stated in Ludwig's third definition [45].

1) *Without Dielectric*: In Fig. 13, the simulated and measured feed patterns without dielectric over 1–20 GHz are presented for co- and cross-polarization in D-plane which is the 45-degree plane between the principal planes (E and H). Good agreement is seen over frequency, acknowledging the perpendicular alignment precision between quarters. Very similar results are seen for both polarizations. The asymmetry caused by the offset coaxial ports is likely to contribute to the small asymmetries seen even in the predicted feed patterns.

2) *With Dielectric*: The polyimide dielectric load with stepped profile was inserted in the QRFH (Fig. 16a) and the feed patterns were measured again with the same chamber setup as without dielectric. Simulated and measured D-plane

patterns are presented in Fig. 13. The agreement is good up to 7 GHz whereafter an unexpected deviation in beamwidth compared to simulated occurs in H-plane but also in E-plane from 13.5 GHz and onward. It is clear from comparing simulated and measured taper at  $60^\circ$ , that this is not apparent before the dielectric is inserted, see Fig. 14. The deviation can be explained by a lower relative permittivity in the material than expected. Straightforward simulations with  $\epsilon_r = 3.1$  confirms this and is presented in the right plot of Fig. 14 alongside the nominal modeled  $\epsilon_r = 3.5$ . The exact value of  $\epsilon_r$  in the range of 1–20 GHz for the specific brand of polyimide is unknown. The tabulated data point available is 0.1 MHz with  $\epsilon_r = 3.4$ , see Table X. From combined information available on different forms of PI-based material the expectation was a small to zero variation in  $\epsilon_r$  over frequency, e.g. [46]. In Fig. 15 the effect on aperture efficiency from variable  $\epsilon_r$  is simulated. The results indicate that this dielectric design tolerates a certain variation over frequency from  $\epsilon_r = 3.5$ , and certainly the expected  $\epsilon_r = 3.4$ . It is also clear that the apparent value  $\epsilon_r = 3.1$  is not desired for nominal  $\eta_a$ , and also evident in measured s-parameters. For the feed's performance on the ATA, the lower relative permittivity will not be detrimental. In-fact, the resulting smaller beamwidth slightly improves the efficiency for the smaller  $\theta_c$  of the ATA, see Fig. 11b. In future iterations, suitable material should be selected from measurements of the complex permittivity over the specific frequency range and cryogenic durability. Due to lack of equipment this is not possible for the authors at the time of this work.

#### A. Tolerance - Ridge Skew Port 2

For the second polarization, after the dielectric was installed, there is an unexpected asymmetry in the measured pattern which is skewed for the higher frequencies - most visibly in the E-plane, see Fig. 16c. This indicates that a misalignment between opposing ridges for the second polarization has occurred during dielectric load insertion, as measurements without dielectric showed good match between simulation and measurement for both ports. Both the dielectric and quarter pieces were machined with high precision and within tolerances specified for the majority of the part. However, in the planar ridge transition the thickness measures 0.05-0.08 mm larger than the nominal 2.0 mm, while the dielectric is near the specified nominal value in the corresponding ridge slots. This resulted in a more snug fit than desired, that required more force to insert dielectric between the ridges sliding it in from the top (Fig. 16a). A small offset in the dielectric's slots for the ridges could lead to a slight skew of the relatively thin and wide ridges when it is inserted from the top with force. By ocular inspection from the top this asymmetry is too small to notice. The s-parameter measurements indicate a degraded port isolation at the low-frequency end after dielectric insertion (Fig. 8) which supports the notion of a small misalignment. There is not an indication of severe asymmetry near the excitation point as it would have degraded port-to-port isolation more noticeably across the higher frequencies. This can be understood because the ridge around the excitation

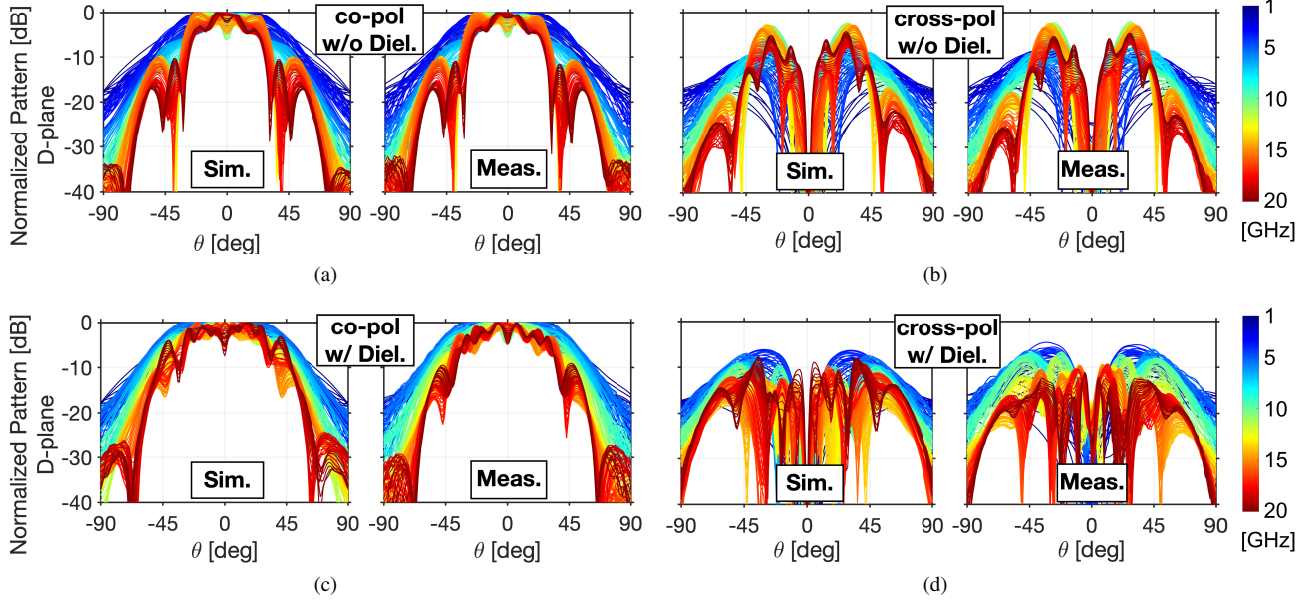


Fig. 13: Simulated and measured normalized feed patterns presented over 1–20 GHz in the diagonal plane (D-plane) **without dielectric** for (a) co-pol.; (b) cross-pol.; and **with dielectric** for (c) co-pol.; (d) cross-pol. Frequency step: 100 MHz.

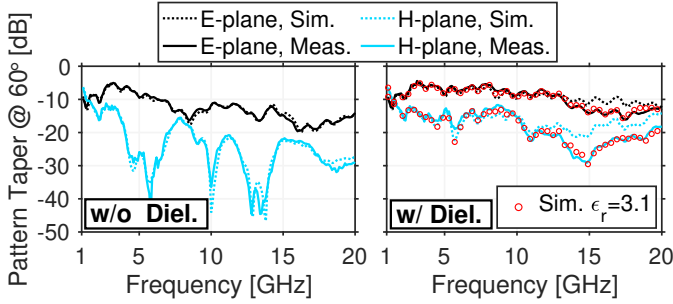


Fig. 14: Simulated and measured pattern taper at  $\theta_e = 60^\circ$ .

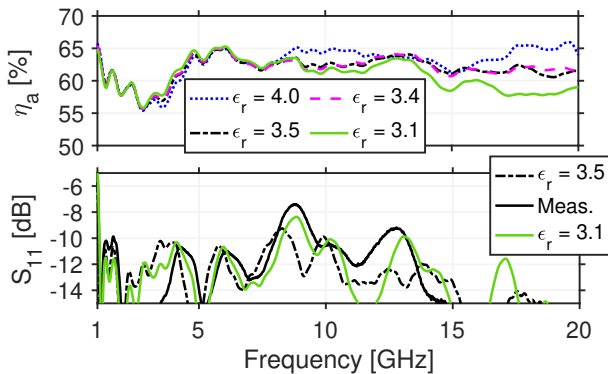


Fig. 15: Simulated effect from  $\epsilon_r$  on  $\eta_a$  ( $\theta_e = 60^\circ$ ) and  $S_{11}$ .

point has better rigidity due to the proximity to the bottom as well as the mechanical reinforcement for the coaxial hole in this region of the ridge. Therefore, the probable explanation is a small asymmetry in ridge-to-ridge alignment somewhere along the analytic transition above the channel where there is less rigidity. At approximately 60 mm above the launch-pins the ridge is 2 mm thick and  $\sim 50$  mm wide which is the likely

point of asymmetry, see Fig. 16a. Such asymmetry is difficult to replicate exactly, but by skewing one of the ridges for the second polarization with  $1.0^\circ$  the error can nearly be replicated in simulation. In this simulation, the relative permittivity was set to  $\epsilon_r = 3.1$  to match the apparent material properties from the manufactured dielectric discovered in Section V-2. In Fig. 16c the replicated error is shown for three frequency points over the range most affected 10, 15, and 20 GHz. The fact that the H-plane symmetry is not further affected indicates that the manufactured dielectric's rotational symmetry is not the culprit. Ocular inspection of the dielectric before and after insertion strengthens this notion. For the same reason, local inhomogeneities in the dielectric material undetectable from the outside is also an unlikely source of error. The margin between ridge and slot can be made bigger without loss of performance to mitigate the risk of misalignment altogether in a future iteration. Additional ridge reinforcement along the horn wall could be investigated as well. The skewed position may relax in a cryogenic environment cycled multiple times, but how this error will affect pointing and efficiency will be studied on-dish compared to the nominal port 1. Simulating the  $1^\circ$  skew suggests a reduction of  $\eta_a$  from 62% to 54% band-average in  $\theta_e = 60^\circ$ , with reduced polarization efficiency.

### B. Feed loss

The feed loss,  $T_{\text{feed}}$ , has been modeled through CST simulations of the radiation efficiency. For low-loss structures the results can vary in accuracy and should be seen as an estimate [47]. In Fig. 17 the simulated feed loss is presented at  $T_{\text{phy}} = 85$  K and the operational temperature  $T_{\text{phy}} = 100$  K used in the cryogenic tests presented in Section VI. The data is smoothed with a 15-point moving average over the 381 frequency points. With the nominal  $\tan\delta = 0.001$  for the polyimide used in this design (Table X), the dielectric



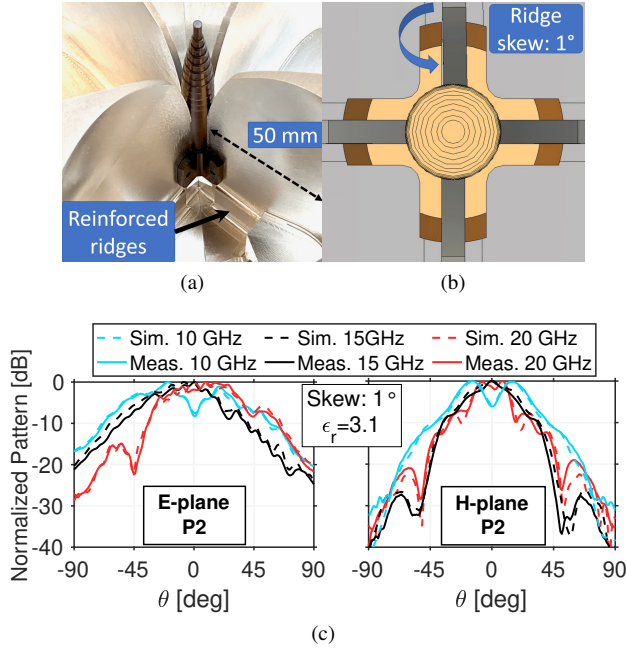


Fig. 16: (a) Dielectric inserted; (b) Illustration of ridge skewing; (c) Simulated skew recreates measured pattern asymmetry.

contributes approximately half of the total loss 8.6 K at 20 GHz assuming uniform  $T_{\text{phy}} = 100$  K over the feed.

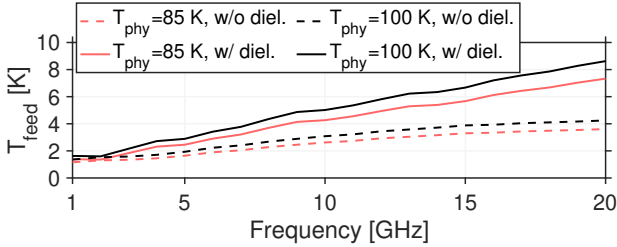


Fig. 17: Simulated feed loss at  $T_{\text{phy}} = 85$  K and 100 K.

## VI. TESTS ON ALLEN TELESCOPE ARRAY

To install and test the dielectrically loaded QRFH in real-world conditions on one of the ATA antennas, the existing cryostat designed for the log-periodic Antonio feed [7] was used. There was a requirement to reuse as many of the existing components and structures as possible, which included the bell-shaped borosilicate glass dome as vacuum enclosure and the copper plate connected to the cryo-cooler via a flexible copper link, see Fig 18a. In the same figure, the aluminum adapter attaching the QRFH to the copper plate is shown. The cryostat operates a Sunpower CryoTel GT Stirling Cooler with enough heat lift to operate the feed horn at 85–100 K (19 W at 85 K). The thermal assembly was modeled in Section III-B. The design of the feed and its supporting components also have to meet several mechanical requirements specifically related to vibrations. Therefore, a number of finite-element simulations in AutoDesk Inventor were carried out to verify that the existing support structures are strong enough to handle

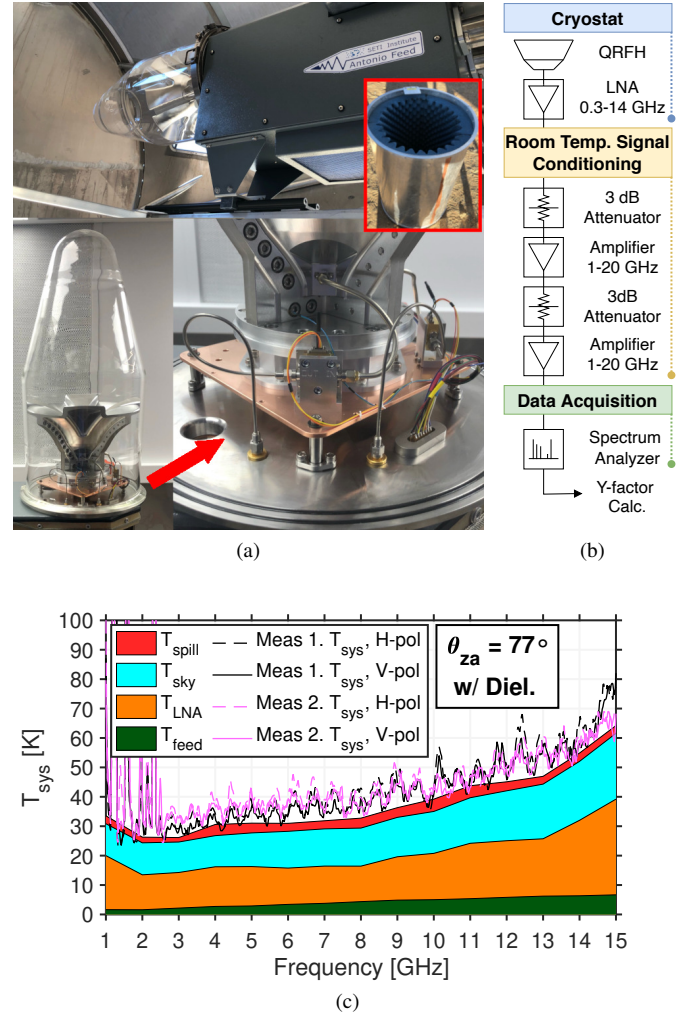


Fig. 18: (a) The dielectrically loaded QRFH in dewar installed on an ATA reflector, LNA seen in center of bottom-right figure. Absorber-bucket for hot load is red inset; (b) Signal chain for Y-factor measurement; (c) Modeled and measured  $T_{\text{sys}}$ , the later for H/V-pol from two different measurements on the ATA. A 5-point moving average used on measured data.

the weight of the QRFH without significant deflection, and with modal-vibration frequencies separated from the forcing frequencies of 60 Hz (cryo-cooler operation) and 120 Hz. Details on these simulations are left out for brevity. The QRFH is connected to the LNAs via two 152 mm long aluminum semi-rigid cables (0.141-inch), see bottom-right of Fig. 18a. The LNAs are supplied with individual datasheet by Low Noise Factory (LNF) and specified nominal over 0.3–14 GHz but functional up to 16 GHz [48]. The authors do not have the possibility to measure the LNAs separately at the operational temperature. Therefore, LNA noise data used in modeling are interpolated with a linear fit to the desired  $T_{\text{phy}}$  from the data available at  $T_{\text{phy}} = 4$  K and 296 K. According to the supplier this is a good approximation. The modeled  $T_{\text{LNA}}$  presented in Fig. 18c is an average of the two LNAs, with individual variation within  $\pm 1$  K. The LNAs are operated with drain bias values of  $V_d = 1.5$  V,  $I_d = 30$  mA specified for  $T_{\text{phy}} = 4$  K



operations. To measure the receiver noise temperature, the hot/cold-method [49] is used where the Y-factor is the output power ratio for two different reference temperatures

$$Y = \frac{P(T_{\text{hot}})}{P(T_{\text{cold}})} = \frac{T_{\text{hot}}}{T_{\text{cold}}}. \quad (5)$$

The cold reference power comprises all the contributions to the system noise power which includes sky, spillover, LNA, and feed noise resulting in  $T_{\text{cold}} = T_{\text{sky}} + T_{\text{spill}} + T_{\text{LNA}} + T_{\text{feed}}$ . The first two components are effectively the antenna noise temperature  $T_a$ , which is calculated as the integral of the power pattern weighted with  $T_b(\theta_{za}, \nu)$ . For the hot reference power, an absorber-bucket (red inset in Fig. 18c) completely covers the glass dome. Therefore, the reference power only has noise contributions from the physical temperature of the absorber,  $T_{\text{abs}}$ , as well as  $T_{\text{LNA}}$  and  $T_{\text{feed}}$ . The  $T_a$  is blocked out resulting in  $T_{\text{hot}} = T_{\text{abs}} + T_{\text{LNA}} + T_{\text{feed}}$ . The component that is present in both reference temperatures is the receiver noise temperature  $T_{\text{rec}} = T_{\text{LNA}} + T_{\text{feed}}$ . By rearranging (5) we can calculate the receiver noise temperature as

$$T_{\text{rec}} = \frac{T_{\text{abs}} - T_a Y}{Y - 1}, \quad (6)$$

where  $Y$  is measured with spectrum analyzer. In Fig. 18b the signal chain for the measurements is presented. In Fig. 18c, the measured  $T_{\text{sys}}$  includes measured  $T_{\text{rec}}$  calculated with (6) added with the modeled  $T_a$ . The absorber temperature  $T_{\text{abs}}$  is accurately determined with a laser thermometer and is 275 K and 276 K for measurements one and two respectively. The largest external uncertainty in the measurement comes from the cold reference, and specifically  $T_a$ . Variations in atmospheric, solar and galactic contributions can be time-dependent over the span of half a day depending on frequency [50]. For the second measurement the reflector was in direct sunlight. The effective ground temperature is another source of uncertainty, depending on soil moisture. Another external uncertainty is potential low-powered RFI adding to the noise. From the Y-factor power spectrum, it is concluded that the peaks seen below 2.5 GHz in Fig. 18c are RFI, as they do not appear in the hot power spectrum (covering the receiver with absorber-bucket). In the modeled receiver noise in Fig. 18c, the LNA is assumed to be at  $T_{\text{phy}} = 80$  K. The measured temperature from the sensor attached to the underside of the copper plate to which the LNAs are attached in measurement, Fig. 18a, was  $T_{\text{phy}} = 79$ –80 K during these measurements. A small temperature difference between LNA and copper plate is possible since no temperature sensor was attached directly to the LNA. An overall uncertainty in the LNA model is from the linear extrapolation used to acquire the modeled data described above. The total estimated uncertainty of the modeled LNA noise is estimated to  $\pm 2.5$  K. The LNA input reflection is more than -5 dB below 3 GHz and above 14.5 GHz which could introduce mismatch loss between the feed and LNA, not included in the modeled noise. Potential losses in the glass dome have not been modeled.  $T_{\text{feed}}$  in Fig. 18c is the modeled loss from Fig. 17 for  $T_{\text{phy}} = 100$  K. During measurement, the temperature sensor for the feed was placed on the outside of the horn, in the bolted connection near the bottom flange,

measuring  $T_{\text{phy}} = 91$ –93 K. This introduces an uncertainty to the inside temperature near the ridge-faces where the dielectric is tightly clamped in-between. The thermal conductivity of the dielectric is much lower than that of the aluminum, and the temperature of the dielectric during operations has not been simulated. Due to time constraints, the prototype feed was not coated with Surtec 650 before the measurements. This increases the overall emissivity specifically with the wire-cut surfaces, and results in a higher heat load on the cryostat when the outside temperature increases. The parts were instead carefully polished after first tests, for temperature stability. The measured  $T_{\text{sys}}$  is less than 45 K in band-average over RFI-free range 2.6–15 GHz at  $\theta_{za} = 77^\circ$  (Fig. 18c). Good agreement is found with the modeled noise within the aforementioned uncertainties. The measurements confirm the low-loss performance of the dielectrically loaded QRFH but to a much higher frequency than other tested systems [51].

## VII. CONCLUSION

The presented dielectrically loaded QRFH feed is an excellent UWB candidate to replace expensive multi-feed receivers over 1–20 GHz in reflector arrays. The QRFH has a single phase-center location making the continuous bandwidth available without re-focusing. The measured band-average input reflection is -13.6 dB and predicted aperture efficiency 62% in a reflector with half-subtended angle  $60^\circ$ . In this paper, the design, manufacture, and measurement of the first prototype have been presented including  $T_{\text{sys}}$  tests with cryogenic LNAs on the ATA, confirming predicted performance. The dielectric load is made from low-loss, space graded polyimide suitable for cryogenic application which improves beamwidth and cross-polarization over frequency compared to the traditional QRFH. At an operational temperature of 100 K the feed is expected to contribute 1.8–8.6 K to  $T_{\text{sys}}$  over the band. For improved low-frequency cross-polarization, an analytic-spline-hybrid ridge profile is implemented using 3D-cubic splines.

## ACKNOWLEDGMENT

The authors would like to thank Pavlo Krasov for assisting during the feed pattern tests. Magnus Dahlgren for assisting with s-parameter tests. Magnus Kjerling for manufacture of bottom flange and test fixture. Mike Taccon, Joe Taccon, and Andy Stokes for advice and manufacture of the quarters. Felix Mannerhagen for advice on manufacture of the dielectric.

## REFERENCES

- [1] P. E. Dewdney, W. Turner, R. Millenaar, R. McCool, J. Lazio, and T. J. Cornwell, "SKA1 System Baseline Design (SKA-TEL-SKO-DD-001)," Mar. 2013. [Online]. Available: [https://www.skatelescope.org/wp-content/uploads/2012/07/SKA-TEL-SKO-DD-001-1\\_BaselineDesign1.pdf](https://www.skatelescope.org/wp-content/uploads/2012/07/SKA-TEL-SKO-DD-001-1_BaselineDesign1.pdf)
- [2] M. McKinnon, C. Carilli, and T. Beasley, "The Next Generation Very Large Array," in *Proc. SPIE*, vol. 9906, Jul. 2016, p. 990627.
- [3] J. Welch *et al.*, "The Allen Telescope Array: The First Widefield, Panchromatic, Snapshot Radio Camera for Radio Astronomy and SETI," *Proc. IEEE*, vol. 97, no. 8, pp. 1438–1447, Aug. 2009.
- [4] A. Niell *et al.*, "Demonstration of a Broadband Very Long Baseline Interferometer System: A New Instrument for High-Precision Space Geodesy," *Radio Sci.*, vol. 53, no. 10, pp. 1269–1291, 2018.

- [5] J. Yang *et al.*, "Cryogenic 2–13 GHz Eleven Feed for Reflector Antennas in Future Wideband Radio Telescopes," *IEEE Trans. Antennas Propag.*, vol. 59, no. 6, pp. 1918–1934, Jun. 2011.
- [6] G. Cortes-Medellin, "Non-Planar Quasi-Self-Complementary Ultra-Wideband Feed Antenna," *IEEE Trans. Antennas Propag.*, vol. 59, no. 6, pp. 1935–1944, Jun. 2011.
- [7] W. J. Welch *et al.*, "New Cooled Feeds for the Allen Telescope Array," *Publ. Astron. Soc. Pacific*, vol. 129 045002, no. 974, Mar. 2017.
- [8] K. A. Abdalmalak *et al.*, "Ultrawideband Conical Log-Spiral Circularly Polarized Feed for Radio Astronomy," *IEEE Trans. Antennas Propag.*, vol. 68, no. 3, pp. 1995–2007, Mar. 2020.
- [9] X. Du, T. Johnson, T. Landecker, and B. Veidt, "An Ultrawideband Nested Coaxial Waveguide Feed Antenna for Radio Astronomy," *IEEE Trans. Antennas Propag.*, vol. 70, no. 4, pp. 2499–2509, Apr. 2022.
- [10] A. Akgiray, S. Weinreb, W. A. Imbriale, and C. Beaudoin, "Circular Quadruple-Ridged Flared Horn Achieving Near-Constant Beamwidth Over Multioctave Bandwidth: Design and Measurements," *IEEE Trans. Antennas Propag.*, vol. 61, no. 3, pp. 1099–1108, Mar. 2013.
- [11] T. S. Beukman, P. Meyer, M. V. Ivashina, and R. Maaskant, "Modal-Based Design of a Wideband Quadruple-Ridged Flared Horn Antenna," *IEEE Trans. Antennas Propag.*, vol. 64, no. 5, pp. 1615–1626, May 2016.
- [12] B. Dong, J. Yang, J. Dahlström, J. Flygare, M. Pantaleev, and B. Billade, "Optimization and Realization of Quadruple-ridge Flared Horn with New Spline-defined Profiles as a High-efficiency Feed over 4.6–24 GHz," *IEEE Trans. Antennas Propag.*, vol. 67, no. 1, pp. 585–590, Jan. 2019.
- [13] J. Flygare *et al.*, "Sensitivity simulation and measurement of the SKA Band 1 wideband feed package on MeerKAT," in *Proc. 13th Eur. Conf. Antennas Propag. (EuCAP)*, Krakow, Poland, Apr. 2019.
- [14] J. Shi, S. Weinreb, W. Zhong, X. Yin, and M. Yang, "Quadruple-Ridged Flared Horn Operating From 8 to 50 GHz," *IEEE Trans. Antennas Propag.*, vol. 65, no. 12, pp. 7322–7327, Dec. 2017.
- [15] K. Kotze and P. Meyer, "Improving Modal Purity in Quadraxially Fed Quadruple-Ridged Flared Horn Antennas," in *Proc. 14th Euro. Conf. Antennas Propag. (EuCAP)*, Mar. 2020.
- [16] A. Dunning, M. Bowen, M. Bourne, D. Hayman, and S. L. Smith, "An ultra-wideband dielectrically loaded quad-ridged feed horn for radio astronomy," in *Proc. IEEE-APS Conf. Antennas Propag. Wireless Commun. (APWC)*, Turin, Italy, Sep. 2015, pp. 787–790.
- [17] H. Lai, R. Franks, D. Kong, D. Kuck, and T. Gackstetter, "A broad band high efficient quad ridged horn," in *1987 Antennas Propag. Soc. Int. Symp.*, vol. 25, Jun. 1987, pp. 676–679.
- [18] T. Satoh, "Dielectric-loaded horn antenna," *IEEE Trans. Antennas Propag.*, vol. 20, no. 2, pp. 199–201, Mar. 1972.
- [19] J. Flygare and M. Pantaleev, "Dielectrically Loaded Quad-Ridge Flared Horn for Beamwidth Control over Decade Bandwidth - Optimization, Manufacture, and Measurement," *IEEE Trans. Antennas Propag.*, vol. 68, no. 1, pp. 207–216, Jan. 2020.
- [20] C. Granet, "Profile Options for Feed Horn Design," in *Proc. IEEE Asia-Pacific Microw. Conf.*, Sydney, NSW, Aust., Dec. 2000, pp. 1448–1451.
- [21] J. Flygare, M. Pantaleev, and S. Olvhammar, "BRAND: Ultra-Wideband Feed Development for the European VLBI Network - A Dielectrically Loaded Decade Bandwidth Quad-Ridge Flared Horn," in *Proc. 12th Euro. Conf. Antennas Propag. (EuCAP)*, London, UK, Apr. 2018.
- [22] K. W. Smart *et al.*, "Pattern Measurements of Cryogenically Cooled Ultra-Wideband Feed Horn," *Proc. 13th Eur. Conf. Antennas Prop. (EuCAP)*, Apr. 2019.
- [23] P.-S. Kildal, "Factorization of the feed Efficiency of Paraboloids and Cassegrain Antennas," *IEEE Trans. Antennas Propag.*, vol. 33, no. 8, pp. 903–908, Aug. 1985.
- [24] J. Yang, "Calculation of Aperture Efficiency of Reflector Antenna with the Measured Far-field Function of its Feed in Ludwig's Third Definition," in *Proc. 15th Eur. Conf. Antennas Propag. (EuCAP)*, Dusseldorf, Germany, Mar. 2021.
- [25] ITP Aero, "Esatan-thermal modelling suite," 2021. [Online]. Available: <https://www.esatan-tms.com/products/catdescription.php?ID=7>
- [26] European Cooperation for Space Standardization (ECSS), *Thermal design handbook – Part 4: Conductive Heat Transfer*. ECSS, 2011.
- [27] National Institute of Standards and Technology (NIST), "Cryogenic material property database," 2022. [Online]. Available: <https://trc.nist.gov/cryogenics/materials/materialproperties.htm>
- [28] D. G. Gilmore, *Spacecraft Thermal Control Handbook*, 2nd ed. Aerospace Press, 2002, vol. 1.
- [29] Azo Materials (Azom), "Borosilicate glass (pyrex/duran) - goodfellow datasheet," 2009. [Online]. Available: <https://www.azom.com/article.aspx?ArticleID=4765>
- [30] Surtec, "Surtec 650," 2022. [Online]. Available: <https://www.surtec.com/en/products-services/surtec-650/>
- [31] C. Kittel, *Introduction to Solid State Physics*. John Wiley, 2007.
- [32] Ensinger, "TECASINT 2011 - Datasheet," 2022. [Online]. Available: <https://www.ensingerplastics.com/en/shapes/products/polyimide-tecasint-2011-natural>
- [33] DuPont, "Vespel SP-1," 2022. [Online]. Available: <https://www.dupont.com/content/dam/dupont/amer/us/en/vespel/public/documents/en/VPE-A10861-00-B0614.pdf>
- [34] Avient, "Preperm Standard Grade - PPE350," 2022. [Online]. Available: <https://www.preperm.com/products/raw-materials/>
- [35] H. Manh Cuong, N. Trong Duc, and V. Van Yem, "Measurement of Complex Permittivity of Materials Using Electromagnetic Wave Propagation in Free Space and Super High-Resolution Algorithm," in *2017 Int. Conf. Adv. Technol. Commun. (ATC)*, Quy Nhon, Vietnam, Oct. 2017, pp. 156–160.
- [36] Ensinger, "TECASINT Compendium - Stock Shapes, Direct Forming," 2022. [Online]. Available: <https://www.ensingerplastics.com/en/-/media/ensinger/files/document-teaser-files/brochures/sintered-plastics/brochure-sp-tecasint-compendium-en.aspx>
- [37] P.-S. Kildal, J. Yang, and M. Ivashina, "New BOR1 and Decoupling Efficiencies for Characterizing Ultra-Wideband Reflectors and Feeds for Future Radio Telescopes," in *Proc. 5th Euro. Conf. Antennas Propag. (EuCAP)*, Rome, Italy, Apr. 2011, pp. 3712–3714.
- [38] G. Cortes-Medellin, "MEMO 95 Antenna noise temperature calculation," pp. 1–13, Jul. 2007. [Online]. Available: [https://www.skatelescope.org/uploaded/6967\\_Memo\\_95.pdf](https://www.skatelescope.org/uploaded/6967_Memo_95.pdf)
- [39] D. I. L. de Villiers and R. Lehmsiek, "Rapid Calculation of Antenna Noise Temperature in Offset Gregorian Reflector Systems," *IEEE Trans. Antennas Propag.*, vol. 63, no. 4, pp. 1564–1571, Apr. 2015.
- [40] R. Lehmsiek and D. I. L. de Villiers, "An Optimal 18 m Shaped Offset Gregorian Reflector for the ngVLA Radio Telescope," *IEEE Trans. Antennas Propag.*, vol. 69, no. 12, pp. 8282–8290, Dec. 2021.
- [41] R. Lehmsiek, I. P. Theron, and D. I. L. de Villiers, "Deriving an Optimum Mapping Function for the SKA-Shaped Offset Gregorian Reflectors," *IEEE Trans. Antennas Propag.*, vol. 63, no. 11, pp. 4658–4666, Nov. 2015.
- [42] A. Pellegrini *et al.*, "MID-Radio Telescope, Single Pixel Feed Packages for the Square Kilometer Array: An Overview," *IEEE J. Microw.*, vol. 1, no. 1, pp. 428–437, Jan. 2021.
- [43] T. D. Carozzi and G. Woan, "A Fundamental Figure of Merit for Radio Polarimeters," *IEEE Trans. Antennas Propag.*, vol. 59, no. 6, pp. 2058–2065, Jun. 2011.
- [44] B. Derat, G. F. Hamberger, and F. Michaelsen, "On the Minimum Range Length for Performing Accurate Direct Far-Field Over-the-Air Measurements," in *2019 Antenna Meas. Techn. Assoc. Symp. (AMTA)*, San Diego, CA, USA, Oct. 2019.
- [45] A. C. Ludwig, "The Definition of Cross Polarization," *IEEE Trans. Antennas Propag.*, vol. 21, no. 1, pp. 116–119, Jan. 1973.
- [46] A. I. Harris, M. Sieth, J. M. Lau, S. E. Church, L. A. Samoska, and K. Cleary, "Note: Cryogenic microstripline-on-Kapton microwave interconnects," *Rev. Scientific Instrum.*, vol. 83, no. 8, Aug. 2012.
- [47] R. Maaskant, D. J. Bekers, M. J. Arts, W. A. Van Cappellen, and M. V. Ivashina, "Evaluation of the Radiation Efficiency and the Noise Temperature of Low-Loss Antennas," *IEEE Antennas Wireless Propag. Lett.*, vol. 8, pp. 1166–1170, Oct. 2009.
- [48] Low Noise Factory (LNF), "Lnf-Inc0.3\_14a," 2022. [Online]. Available: <https://www.lownoisefactory.com/products/cryogenic/03-14a/>
- [49] D. M. Pozar and B. Kaufman, "Comparison of Three Methods for the Measurement of Printed Antenna Efficiency," *IEEE Trans. Antennas Propag.*, vol. 36, no. 1, pp. 136–139, Jan. 1988.
- [50] G. J. Hovey, R. Messing, A. G. Willis, and B. Veidt, "An Automated System for Measurement of Sensitive Microwave Radiometers," in *18th Int. Symp. Antenna Technol. Appl. Electromagn. (ANTEM)*, Aug. 2018.
- [51] G. Hobbs *et al.*, "An ultra-wide bandwidth (704 to 4 032 mhz) receiver for the parkes radio telescope," *Publ. Astron. Soc. Aust.*, vol. 37, Apr. 2020.